Research Article Vol. 14, No. 12 / 1 Dec 2023 / Biomedical Optics Express 6328
Biomedical Optics EXPRESS

Real-time OCT feedback-controlled RPE photodisruption in ex vivo porcine eyes using 8 microsecond laser pulses

CHRISTIAN BURRI,[1,2,*] SIMON SALZMANN,[1] JASMIN WANDEL,[3] LEONIE HOFFMANN,[1] BORIS POVAŽAY,[1] CHRISTOPH MEIER,[1] AND MARTIN FRENZ[2]

[1] optoLab, Institute for Human Centered Engineering, Bern University of Applied Sciences, Biel, Switzerland
[2] Biomedical Photonics Group, Institute of Applied Physics, University of Bern, Bern, Switzerland
[3] Institute for Optimisation and Data Analysis, Bern University of Applied Sciences, Burgdorf, Switzerland
[*] christian.burri@bfh.ch

Abstract: Selective retinal pigment epithelium (RPE) photodisruption requires reliable real-time feedback dosimetry (RFD) to prevent unwanted overexposure. In this study, optical coherence tomography (OCT) based RFD was investigated in ex vivo porcine eyes exposed to laser pulses of 8 µs duration (wavelength: 532 nm, exposure area: $90 \times 90\,\mu m^2$, radiant exposure: 247 to 1975 $mJ/\mu m^2$). For RFD, fringe washouts in time-resolved OCT M-scans (central wavelength: 870 nm, scan rate: 85 kHz) were compared to an RPE cell viability assay. Statistical analysis revealed a moderate correlation between RPE lesion size and applied treatment energy, suggesting RFD adaptation to inter- and intraindividual RPE pigmentation and ocular transmission.

1. Introduction

The retinal pigment epithelium (RPE), a highly specialized polarized monolayer between the neuroretina and the nourishing underlying choroid, has a major impact on retinal health and diseases [1–3]. It's apical membrane faces the photoreceptor outer segments and interphotoreceptor matrix [4], whereas the RPE's basal lamina is part of Bruch's membrane [1]. Furthermore, tight junctions between neighboring RPE cells complete the outer blood-retinal barrier. This dynamic gate regulates the extracellular milieu of the developing retina, and later of the mature photoreceptors [5]. Some of the most important functions of the RPE cells are the regulation of heat exchange, ion balance, light absorption (protection against photo-oxidation, as well as increased optical quality via reduced back scatter), and active transport of molecules into, out of, and through the RPE [6]. Furthermore, cyclic shedding of photoreceptor outer segment material is phagocytosed by the RPE [7] and the RPE maintains the immune privilege of the eye [8,9]. RPE cells also produce various growth factors and are considered the major source of the vascular endothelial growth factor (VEGF) of the outer retina [10]. Therefore, it is not surprising that an RPE dysfunction is associated with a variety of retinal diseases. Disruption of the homeostatic balance between the choroid, RPE and neural retina causes many of the most common retinal diseases. For example, age-related RPE changes appear to be closely associated with the development of age-related macular degeneration (AMD) [11]. Furthermore, diseases like central serous chorioretinopathy [12] or diabetic macular edema are associated with reduced RPE function [13].

Fortunately, its intrinsic epithelial resilience and regenerative capacity has prompted the development of numerous regenerative retinal laser and light therapies (RELITE) to induce a stimulation of the photoreceptor / RPE / choroid complex without inducing functional or structural neuroretinal and choroidal damage [14]. Thereby, the photodisruptive laser approach known as selective retina therapy (SRT) which induces RPE rejuvenation was found to be particularly

#503941 https://doi.org/10.1364/BOE.503941
Journal © 2023 Received 22 Aug 2023; revised 24 Oct 2023; accepted 12 Nov 2023; published 20 Nov 2023

Biomedical Optics EXPRESS

suitable [15]. SRT intends to selectively initiate immediate cell disruption of dysfunctional or senescent patches of the approximately 10 µm thick RPE monolayer without scarring the choroid and neurosensory retina, and especially sparing the non-regenerative photoreceptors, to enable RPE-mitosis, regrowth, and uptake of physiological retinal function [15,16]. The basis for selective laser damage is the RPE's high melanin content in the intracellular melanosomes, which absorb about 50% of the incident light in the green spectral range in their function as stray-light suppressors [6,17]. Within the thermal confinement of the relatively short microsecond-long pulses used for SRT, high peak temperatures (140 to 150 °C) at the melanosomes in the RPE initiate intracellular, and later the coalescence microsecond-long microbubble formation (MBF) [18–20]. Rapid mechanical expansion, and collapse of these micrometer-sized steam bubbles successively cause RPE cell wall disruption, followed by immediate or delayed cell death [19].

Various clinical studies have already demonstrated clinical efficacy of SRT for the treatment of RPE related retinal diseases such as macular edema (DME, macular edema secondary to retina vein occlusion, Irvine-Gass Syndrome) [21–25]. Furthermore, clinical efficacy of SRT has been successfully demonstrated in various clinical trials for the treatment of CSCR [12,26–31]. Recently, Kim et al. were even able to show first success by treating intermediary age-related macular degeneration (iAMD) patients with SRT [32]. However, for a clinically successful application of SRT there are some hurdles that have to be overcome. In detail, our target tissue, especially pathologic but also physiologic RPE, is not uniform and partially covered by absorbing retinal vasculature. The morphometry of RPE cells changes with age, by becoming less dense, larger, and losing their typical hexagonal shape [33]. However, more important, regarding laser treatment applications, is the circumstance, that RPE cells have a strongly varying melanin concentration. On the basis of post mortem analyzed human eyes, Schmidt and Robert showed that the concentration of melanin is the lowest within the macula [34]. Compared to the mid-periphery, the concentration is lower by a factor of about two. In comparison to the far-periphery, the difference is even about a factor of three. This value was partly reflected even in single individuals where the melanin concentration within the fundus varied up to a factor of 3.2 between the macula and far-periphery. Furthermore, there is a trend of a decreasing melanin concentration in the mid- and far-peripheral regions with age [35]. In addition, the transparency of the human eye decreases as well by several tens of percent with age [36,37]. This leads to strongly varying inter- and intraindividual thresholds for selective RPE cell damage. Therefore, reliable real-time feedback dosimetry (RFD) is essential to preserve photoreceptor integrity during the laser treatment. Hence, several approaches for real-time SRT control respectively real-time MBF detection are under development. Delivering real-time feedback on the localized impact is imperative for keeping the laser energy within a treatment window, at best without additional mechanical interaction to minimize the procedure's invasiveness. Therefore, methods such as measuring the increased reflectance at the bubble surface via backscattered light or capturing the ultrasonic emission caused by rapid bubble expansion and collapse to detect the presence of MBF have been investigated and successfully tested [38,39].

Another promising SRT dosimetry approach is the utilization of optical coherence tomography (OCT). OCT has been developed for non-invasive cross-sectional imaging in biological systems and uses scanning low-coherence interferometry to produce depth-resolved images of optical backscatter originating from local discontinuities of the refractive index within tissue microstructures [40]. In the last two decades, OCT has become an integral part of clinical ophthalmology, providing detailed anatomical and morphological information, especially of the retina [41]. In terms of RFD laser control, OCT was already evaluated for continuous-wave laser photocoagulation [42]. There the goal was to guarantee predictable coagulation strength and size as well as to provide safer and more reproducible treatments. Thermal tissue expansion and scattering changes were assessed in time-resolved OCT A-scans (M-scans). For SRT, a similar method was described by Steiner et al., who indirectly detected tissue effects of laser pulses as

Biomedical Optics EXPRESS

OCT-signal loss in OCT M-scans [43–45]. The detailed mechano-optical model of the signal loss during laser treatment is still debated, but the currently favored hypothesis explains it as interference signal contrast loss, or decorrelation, also known as "coherence fringe washout" resulting from the fast motion or other signal alterations of the monitored retinal surfaces due to MBF within time scales of and above the coherent acquisition time of the depth scan [46]. In consideration are axial motion during thermal expansion as well as fast dynamic changes of the scattering behavior during the transition from thermal expansion to MBF, leading to an OCT signal attenuation at the level of the RPE. However, the most prominent explanation for a fringe washout and thus a signal-to-noise ratio (SNR) penalty of nearly 100% is the strong axial motion (vibration) during MBF itself. For RPE irradiation in SRT with short microsecond pulses, the collapse of microbubbles generates pressure waves with velocities up to 30 m/s [20]. The chaotic phase fluctuation caused by the vibration leads to a complete signal loss throughout the entire retina over the duration of a single A-scan within the acquisition time of the interferometric measurement of typically 10 to 30 µs or longer depending on the input energy and lifetime of the microbubbles of a few microseconds. This roughly corresponds to the average cumulative microsecond lifetime of MBF during SRT [19] and is, as we have recently shown, also consistent with the occurrence of OA transients during RPE damage [47]. Notably, these fringe washouts across the entire retina cannot be assimilated to a laser-tissue interaction across the entire retina but originate in the RPE.

In terms of RFD, Burri et al. recently presented an SD-OCT-based dosimetry algorithm for SRT [46]. For certain ex vivo porcine retina samples, this algorithm achieved a sensitivity of 99% and specificity of 97% for predicting RPE lesions after microsecond laser application. The Spectralis Centaurus device (HuCE-optoLab, Bern University of Applied Sciences, Biel, CH) used in this experiment is currently also being evaluated at the Department of Ophthalmology at the Bern University Hospital (Inselspital, Bern, CH). With laser pulses of 8 µs duration, the potential, procedure, and feasibility of the dosimetry algorithm used have been recently demonstrated by Burri and Dysli et al. in the first three patients with diabetic retinopathy [48,49]. Furthermore, details of RPE regeneration after SRT were presented using High-Res-OCT (Heidelberg Engineering, Heidelberg, DE) with 3 µm axial resolution [50]. However, in this patient study, the RFD algorithm is evaluated post-treatment without real-time application. In parallel first promising in vivo real-time SRT dosimetry results were obtained in experiments with rabbits [51] as well as pigs [52]. A subgroup of lesions in a range of test-patterns were successfully controlled by RFD at different pulse durations. Thereby, we demonstrated that OCT-based RFD can interrupt the treatment laser in real-time for each lesion, resulting in controlled and accurately dosed RPE damage. In some cases, this algorithm limited the applied number of pulses to 4 of 15 planned pulses with increasing exposure (ramp-mode), which resulted in an energy deposition reduction of 83% in the retina whilst keeping a clearly defined RPE damage profile, according to fluorescence angiography.

In the experiment shown here, we have used the same method and algorithm again to study OCT-based RFD. Extending our previous work, we apply the algorithm for the first time in a large 75-lesion pattern using real-time dosimetry. Thereby, we demonstrate that OCT M-scan based RFD enables controlled photodisruption of the RPE without detectable adjacent morphologic tissue damage or other suprathreshold laser effects.

2. Materials and methods

2.1. Treatment and monitoring system

For the experiments, the non-commercially available research device Spectralis Centaurus (HuCE-optoLab, Bern University of Applied Sciences, Biel, CH) was used [53]. This device is based on a modified diagnostic imaging platform (Spectralis, Heidelberg Engineering, Heidelberg, DE), extended with a prototype treatment laser (modified Merilas 532 shortpulse, Meridian Medical,

Biomedical Optics EXPRESS

Thun, CH) intended for SRT. The laser emits radiation at 532 nm, supports pulse durations from 2 to 20 µs at a repetition rate of 100 Hz, and delivers 30 W power [54]. The laser beam was shaped to a square beam profile and focused to a spot size of approximately 90×90 µm^2 (8100 µm^2) onto the porcine retina. Thereby, an intensity modulation factor (IMF) of 1.3 is achieved, indicating an almost homogeneous top-hat beam profile [55]. The IMF describes the ratio of maximum to mean radiant exposure across the beam profile [56]. An IMF of 1 corresponds to perfectly homogenous, top-hat radiant exposure. Furthermore, the system features the ability of intervention planning utilizing the integrated confocal scanning laser ophthalmoscope (cSLO) and a spectral-domain (SD) - also known as Fourier-domain (FD) OCT. The super-luminescence diode of the SD-OCT laser emits broadband infrared radiation centered at 870 nm wavelength with a 73 nm spectral bandwidth. The high-speed spectrometer of the OCT system is operated at a rate of 85 kHz resulting in an integration time of 11.8 µs per A-scan. In B-scan mode the beam scans across the retina, producing a cross-sectional, depth resolved backscatter-image from minute interfaces to acquire the tissue micromorphology. Furthermore, it can be operated in the so-called M-scan-mode (motion-mode). This mode measures time-resolved sequences of A-scans at the point of the treatment laser application without scanning, thereby unveiling depth-resolved temporal signal fluctuations including signal loss (coherent fringe washouts) for RFD (Fig. 1).

The applied pulse number was monitored with an integrated photodiode (VEMD5510CF, Vishay Intertechnology, US). This monitoring diode is located behind the dichroic mirror (transmission 0.1%) through which the SRT laser is coupled into the OCT beam path. The acquired laser parameters are stored together with the settings and the feedback of the dosimetry algorithm in a treatment record file. The treatment can thus be accurately tracked and later evaluated for each individual lesion.

With respect to clinical application and considering a static OCT beam for M-scan recording the OCT illumination power after the delivery optics was limited to <0.85 mW within the accessible emission limit for class 1 laser products, complying with standard IEC 60825-1 (Safety of laser products. Equipment classification and requirements).

2.2. Tissue preparation

Juvenile porcine eyes were used for the experiments due to availability. Porcine eyes resemble the human eye in anatomic and physiologic characteristics better than any other mammalian eye, except for non-human primates, especially with regard to size, cone distribution and retinal layers [57–59]. The porcine retina has a rod-enriched periphery and a cone-enriched area centralis, also referred as visual streak (VS), that resembles the human macula [60,61]. Pig eyes were obtained from a local slaughterhouse (pigs ≈ 24 weeks old, ≈ 110 kg). After enucleation, the eyes were transported to the laboratory (< 30 minutes) in a jar filled with phosphate-buffered saline (PBS), in a cooled thermo box (freshly enucleated eyes should be kept at 4°C [59]). Before treatment, superfluous connective tissue was removed from around the eyeball.

For irradiation, the eyes were positioned in a special 3D-printed plastic container (polylactic acid (PLA), Ultimaker S5, Utrecht, NL) attached to the original head rest in front of the delivery optics of the treatment system.

To maintain the intraocular pressure (IOP), an intravitreal injection into the vitreous cavity through the pars plana was made. The pars plana, located 4 mm from the limbus (cornea/sclera junction), is a safe area at the end of retinal tissue (ora serrata) to penetrate the eye wall with a needle. The eyes were cannulated using a disposable hypodermic needle (20 G × 1 1/2", Teqler, Wecker, LU) connected with a tube to a height adjustable column filled with balanced salt solution (BSS). A physiological pressure transducer (SP844, Memscap, Isere, FR), inserted in the silicon tube at the same height as the eye via an attached silicon diaphragm dome (844-28, Memscap, Isere, FR), allowed the recording, respectively the control of the IOP. The eyes were

Biomedical Optics EXPRESS

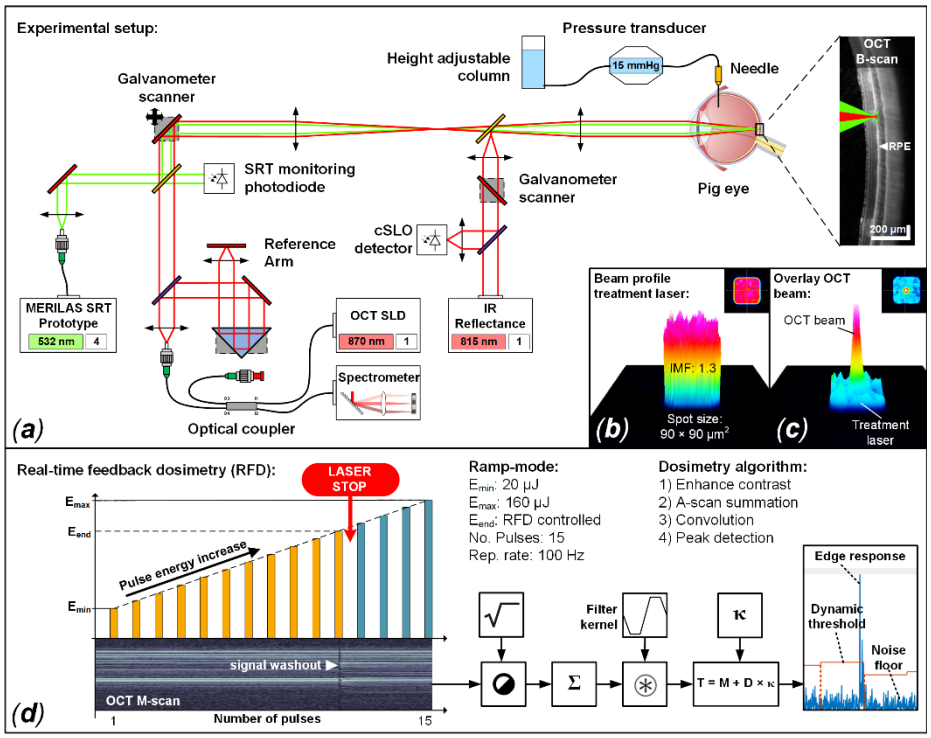

Fig. 1. Experimental setup and functionality of the Spectralis Centuarus device and real-time feedback dosimetry (RFD) algorithm: (a) the SD-OCT (870 nm) and treatment laser (532 nm) beams are aligned coaxially by a dichroic mirror. Behind the dichroic mirror, the treatment laser is detected by an avalanche photodetector. Retina scanning for OCT imaging and treatment laser application is performed by a galvanometric scanner. A chromatically corrected objective focused the collinear treatment and OCT laser beams to ex vivo porcine retinas. The Spectralis's standard integrated IR cSLO eases treatment planning by displaying a fundus image for interactive treatment pattern placement. The treatment spot size on the porcine retinas was about 90×90 µm^2 superimposed with the centered Gaussian OCT beam (b, c). (d) ramp-mode and RFD: within the RFD probe region pulse bursts (15 pulses; 100 Hz repetition rate) with increasing pulse energy from 20 µJ (247 mJ/cm^2) to 160 µJ (1975 mJ/cm^2) were applied. For RFD, the simultaneously to the treatment laser application recorded OCT M-scans were evaluated for fringe washouts by a dedicated dosimetry algorithm. Fringe washouts occur due to the formation of microbubbles in the RPE during laser irradiation near and above the damage threshold. M-scan processing is roughly done in four steps: 1) contrast enhancement, 2) A-scan summation, 3) convolution and 4) peak detection [46]. Whenever a fringe washout was detected, the pulse ramp was interrupted and thus the end energy for a specific lesion individually targeted.

Biomedical Optics EXPRESS

pressurized at 15 mmHg. This corresponds roughly to the IOP found in pigs (15.2 mmHg) [62] and also to the mean IOP of humans (14.7 mmHg) [63]. The cornea was manually moistened with BSS approximately 10 times per minute using BSS. An intact corneal tear film (≈3 µm) is important for maintaining epithelial integrity, physiologically reducing surface scattering and helps to partially correct high order optical aberrations by smoothing out the rough ocular surface (≈130 nm) [64–66]. The experiments took place at room temperature well within the common cellular survivability time window, which should not exceed 5 h [59].

2.3. Treatment pattern and irradiation

As depicted in Fig. 2(a), the porcine retina has, beside a mid- and peripheral region, a rod-enriched periphery and a cone-enriched area centralis [60,61,67]. The laser treatment probe regions for the experiment presented here were always applied within the VS. One advantage of applying the pattern in the VS, in addition to its similarity to the human macula, is that the laser beam path passes relatively centrally through the porcine eye. This is important because the pig eye, compared to humans, can cause relatively strong aberrations in the periphery due its thicker cornea coupled with a larger corneal diameter and radius, and greater corneal astigmatism [68]. To locate the VS area, a wide-angle lens (Widefield Imaging Module, Heidelberg Engineering, Heidelberg, DE) with 55° field of view was used for fundus imaging. Once the desired area was localized (VS area nasal to the optic disc), the delivery optics was switched back to the standard 30° lens for the remaining treatment.

The treatment pattern consisted of a rectangular probe region surrounded by 19 reliably detectable marker lesions (Fig. 2(b, c)). These marker lesions were applied in CW-mode (200 ms pulse duration and 200 mW pulse power) to form easily identifiable white denaturalization spots. Inside this demarcation frame, three spatially separated probe regions were placed: two single pulse probe regions (P1 and P2) as well as an RFD probe region.

A single pulse probe region was placed once above the RFD probe region (P1) and once below (P2). Here, single laser pulses of 8 µs duration were applied while increasing the pulse energy from left 20 µJ (247 mJ/cm^2) to right 160 µJ (1975 mJ/cm^2) for P1 and vice versa from right to left for P2. Thus, the two patterns P1 and P2 differed only by their locally separated arrangement and the direction in which the energy was linearly increased. This locally spread arrangement enabled the detection of intraindividual RPE damage threshold variations and variations in laser absorption, which is important with respect to SRT. P1 and P2 also represented a control (to the RFD probe region) as the pulse energy gradation from the 1st to the 15th lesion exactly matched the range of the applied ramp per lesion in the RFD probe region.

The RFD probe region consisted of a pattern of 75 lesions (15×5). Within this pattern, as shown in Fig. 1(a), a pulse burst (15 pulses, 100 Hz repetition rate) would theoretically be applied at each lesion. Thereby, the applied energy was increased linearly (ramp-mode) from pulse No.1 with 20 µJ (247 mJ/cm^2) to pulse No. 15 with 160 µJ (1975 mJ/cm^2), in the same range as for P1 and P2. However, the ramp was automatically interrupted in real time by the dosimetry algorithm as soon as a fringe washout was detected in the OCT M-scan. In this respect, the ramp's end energy was selected individually for each lesion by the algorithm.

Before the experiment, the pulse energy was measured using a calibrated energy meter (J-10MB-LE, Coherent, Santa Clara, CA, US) in front of the laser aperture of the system.

For each sample, the exposure position of the retina was optimized using coaxially aligned live OCT B-scans prior to laser application. This ensured that each lesion was optimally in focus (due to the confocal arrangement of the treatment laser and OCT beam (Fig. 1(c))), despite aberrations, resulting in optimal treatment laser projection as well as optimal OCT dosimetry feedback. The application of the entire pattern took about 4 minutes. Each treatment spot had to be triggered individually via a foot pedal.

Biomedical Optics EXPRESS

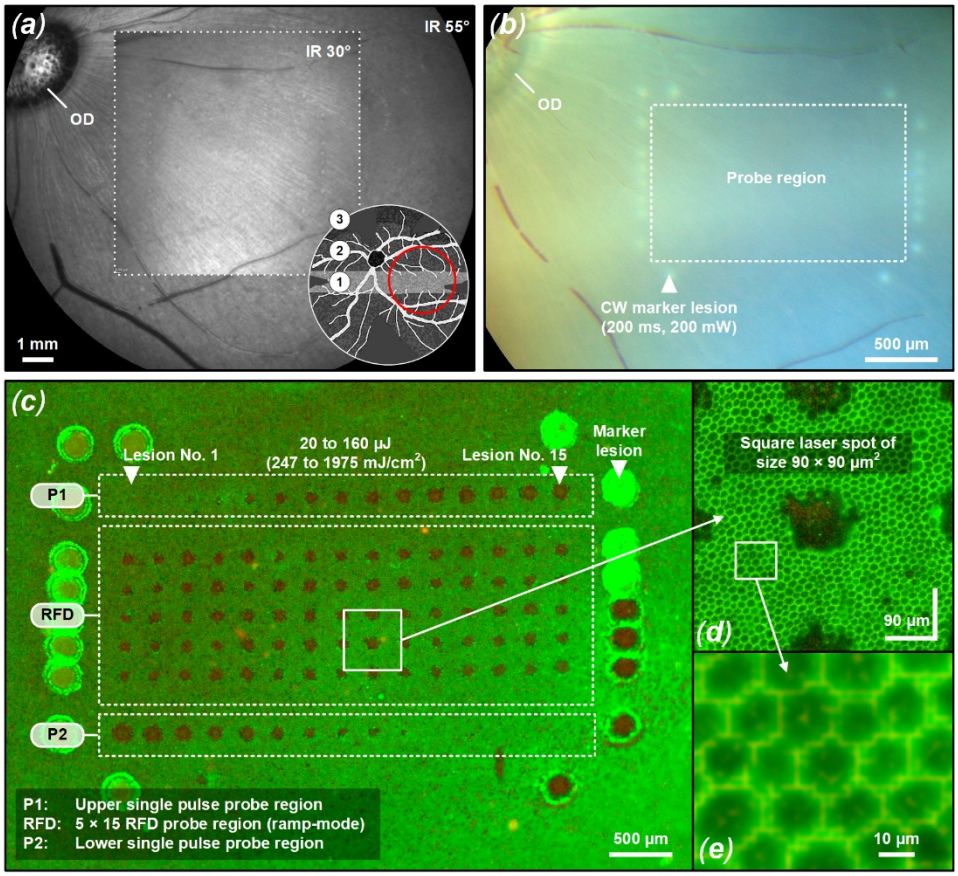

Fig. 2. Post-treatment overview (based on sample No. 3 (1-161)) of the laser application to ex vivo porcine eye retinas. (a) IR cSLO image (30° and 55°) of the pig fundus. The pig retina map shows the IR cSLO 55° FOV (red circle) and the three main retinal regions including vessels (white): visual streak (VS, No. 1: pale gray), midperiphery (No. 2) and periphery (No. 3: gray) according to Garca et al. [67]. The treatment pattern was placed within the VS close to the optic disc (OD). (b) Corresponding CFP image showing 19 marker lesions around the SRT probe region (white-dashed rectangle). (c) Complementary live/dead RPE cell viability assay showing the SRT treatment pattern with three different probe regions. In region P1 and P2, the same single-pulse pattern was applied with linearly increasing laser pulse energy from 20 µJ (247 mJ/cm^2) to 160 µJ (1975 mJ/cm^2). The energy was increased once from left to right and once vice versa from right to left in steps of 10 µJ. A pattern comprising 5×15 lesions was applied in the intermediate RFD probe region. These 75 lesions were controlled by the RFD algorithm. For this purpose, the lesions were applied in ramp mode limited to a maximum of 15 pulses (repetition rate: 100 Hz, E_{min}: 20 µJ, E_{max}: 160 µJ). The ramp exposure sequence was interrupted as soon as a fringe washout was detected in an OCT M-scan by RFD. (d) Magnified image of a lesion corresponding to the applied laser spot size of 90×90 µm^2 (8100 µm^2). (e) Enlarged image showing the typical hexagonal RPE structure. Staining: green-fluorescent calcein-AM (live) and red-fluorescent ethidium homodimer-1 (EthD-1, dead).

Biomedical Optics EXPRESS

2.4. Real-time feedback dosimetry

For better understanding, the broad functionality of the SD-OCT-based RFD algorithm for SRT, which was recently presented by Burri et al. [46], is shown again in Fig. 1(d). In brief, the algorithm functions as follows: the algorithm receives M-scans of ~3 ms duration (consisting of 256 A-scans). Then a contrast enhancement is performed by means of a gamma correction. Next, an A-scan summation and signal filtering is performed, followed by the detection of the edge response. Thereby, the threshold for the detection must be set as variable sensitivity factor (κ-value). This parameter determines the sensitivity ratio between the fringe washout-based filter edge response and the background noise of the M-scan. This detection threshold is dynamic and adapts to the noise floor. In this experiment, a sensitivity of $\kappa = 11$ was chosen for the algorithm. This setting was previously evaluated in different experiments to guarantee reliable detection of fringe washouts in OCT M-scans in ex vivo pig eyes with RPE destruction (high sensitivity). In this experiment, the chosen sensitivity setting of $\kappa = 11$ was validated after the experiment based on the single pulse probe region and compared to 18 other κ-value settings.

2.5. Fundus examinations

Within 30 minutes after laser irradiation, fundus photographs and OCT C-scans were acquired to evaluate morphological changes after laser application. Color fundus photography (CFP) was assessed using a fundus camera (Fundus Module 300, Haag-Streit, Köniz, CH). OCT C-scans were acquired over the treatment region using a pre-defined OCT scan pattern (size: 30°×20° ($8.9 \times 6.0\,mm^2$); number of B-scans: 97; averaged B-scans: 38) to compare morphological changes with RPE lesion formation.

2.6. RPE cell viability assay

After microsecond laser irradiation, viability of RPE cells was evaluated using a two-color assay live/dead staining kit (L3224, Thermo Fisher Scientific, Waltham, US). Therefore, the eyes were carefully cut in half, the vitreous body was removed, and an area encircling the exposure pattern of the visible marking lesions was excised. Successively, the specimens were placed in phosphate-buffered saline (PBS) for 30 minutes to gently detach the retina from the RPE and facilitate complete retinal removal. The specimens were further incubated for 30 minutes at room temperature using the staining kit. The viable-lethal analysis was conducted using a fluorescence microscope (Axio Lab.A1, Carl Zeiss, Oberkochen, DE) and attached microscope camera (Gryphax Progres, Jenoptik, Jena, DE). Thereby, green-fluorescent (emission: 517 nm) calcein-AM (live) and red-fluorescent (emission: 617 nm) ethidium homodimer-1 (EthD-1, dead) as well as bright green hyperfluorescence indicated function or loss of plasma membrane integrity. Post-processing of the fluorescence images was accomplished with the Fiji image processing package distribution of ImageJ [69]. Fiji was also used to measure the size of all applied laser lesions. The lesion sizes were then compared with the applied laser pulse energy and with the shut-off behavior of the RFD algorithm.

2.7. Statistical evaluation

To investigate the inter- and intraindividual RPE damage thresholds in dependence of the applied laser parameters a probit analysis was performed and dose-response percentiles were calculated. The effective dose (ED) is defined as the median dose at which 50% (ED_{50}) of the exposures resulted in a response, i.e. in form of a detectable RPE laser lesion. Correspondingly, exposure doses at which 16% and 84% of the exposures resulted in detected lesions are referred to as ED_{16} and ED_{84}, respectively. The logarithms of these two threshold levels represent one standard deviation in the normal distribution from the logarithm of the median dose [70]. The probit analysis was performed with Origin 2023 (OriginLab Corporation, Northampton, MA) utilizing

Biomedical Optics EXPRESS

the Levenberg Marquardt iteration algorithm to fit with a χ^2 tolerance value of 1×10^{-9} within up to 400 iteration steps. The binary RPE damage evaluation of the two spatially separated single pulse probe regions (P1 and P2) served as input for the probit analysis. Thereby, the criteria for successful damage to the RPE was defined such as the lesion area (including hyperfluorescent cells) had to exceed 50% of the square treatment beam profile of 90×90 µm^2 (8100 µm^2), thus receiving scores of 1 and 0 otherwise.

A binary evaluation was similarly performed for the simultaneously recorded OCT M-scans. Although the algorithm was only actively used for the RFD pattern, the theoretical algorithm performance was also investigated post-treatment for the single pulse probe region (P1 and P2). The ground truth for the statistical evaluation was based on the RPE cell viability assay and the hypothesis that RPE lesions due to MBF lead to fringe washouts in SD-OCT M-scans. Fringe washouts in M-scans were assessed using the dedicated RFD algorithm and by applying 19 different κ-values ranging from 5 to 100. For statistical evaluation, the occurrence of fringe washouts (predictive class) was compared to the damage outcome on the viability assay (actual class) by using the confusion matrix as described by Burri et al. [46]. The confusion matrix features four cardinalities: true positive (TP), true negative (TN), false positive (FP) and false negative (FN). Thereby, positive and negative refer to the prediction (true or false) of whether an RPE lesion was created, based on the presence SD-OCT M-scans fringe washouts. Based on the four cardinalities, several statistical measures were derived to present the overall device performance in a straightforward fashion. In our case, the sensitivity, specificity, accuracy, positive predictive value (PPV) and negative predictive value (NPV) were calculated.

Further, in order to analyze the dependency between the applied laser pulse energy and the resulting laser lesion size, the repeated measures correlation (rmcorr) coefficient [71] was calculated with the corresponding 95% confidence interval. Unlike the Pearson correlation, which assesses the inter-individual association because it assumes each paired data point is independent and identically distributed, rmcorr evaluates the overall or common intra-individual association between two measures. Therefore, the rmcorr coefficient adjusts for the dependency among the repeated measurements within a single specimen. To calculate an appropriate prediction interval for the RFD controlled laser lesions, which accounts for the dependency among the measurements, a generalized mixed effect model was calculated. Using this model, a 95% confidence interval for the corresponding mean laser lesion size could also be calculated.

3. Results

From 750 applied and RFD controlled laser lesions, no RPE damage was found for 8 lesions (1.0%) in the cell viability assay. Among all lesions, the treatment laser (ramp-mode), was deactivated too early for 7 lesions (0.9%), since noise was detected instead of an OCT M-scan fringe washout using an RFD algorithm sensitivity presetting of $\kappa = 11$. These 7 lesions were excluded from further evaluation. For 1 lesion (0.1%) no RPE damage was achieved even with the maximum applied pulse number of 15 and thus the maximum treatment energy of 160 µJ (1975 mJ/cm^2) due to interference with a small blood vessel.

Fig. 3 shows the inter- and intraindividual damage thresholds detected in each sample. The evaluation is based on the RPE cell viability assay on the two single pulse probe regions (P1 and P2) in each sample. A rather high RPE damage threshold of 120 µJ (1481 mJ/cm^2) was determined in four samples (sample No. 1, 2, 9 and 10) and a low threshold of 60 µJ (741 mJ/cm^2) was found in two samples (sample No. 4 and 8). The largest difference of 40 µJ (494 mJ/cm^2) between P1 and P2 within one sample was found for sample No. 1. Here, the damage threshold was 120 µJ (1481 mJ/cm^2) in the lower single pulse probe region (P2) and only 80 µJ (988 mJ/cm^2) in the upper one (P1). In sample No. 8, the same threshold of 100 µJ (1235 mJ/cm^2) was observed in both probe regions. An RPE damage threshold (ED_{50}) of 87 µJ (1074 mJ/cm^2) was determined across all samples.

Biomedical Optics EXPRESS

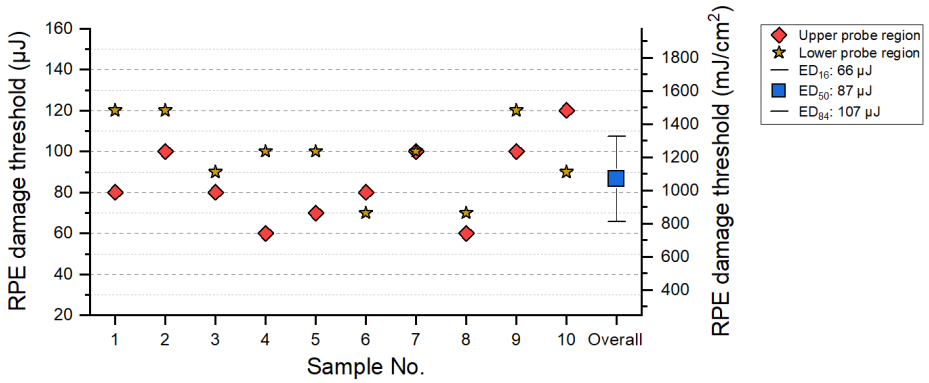

Fig. 3. Results RPE cell viability assay: inter- and intraindividual as well as overall RPE damage threshold based on the upper (P1) and lower (P2) single pulse probe region. Overall, a median RPE damage threshold (ED_{50}) of 87 µJ (1074 mJ/cm^2) was found.

Fig. 4 shows the number of applied pulses in ramp mode per sample. The pulse burst of the ramp consisted of 15 pulses. For sample 1, for example, we see that the treatment laser (ramp) in the RFD sample region was interrupted by the dosimetry algorithm at a median value of 10 pulses. The smallest distribution and thus probably the most homogeneous local treatment conditions were found for sample number 8. Across all samples, the median number of ramp pulses applied was 9 out of 15. Therefore, the energy range setting of 20 to 160 µJ seems to have been chosen appropriately.

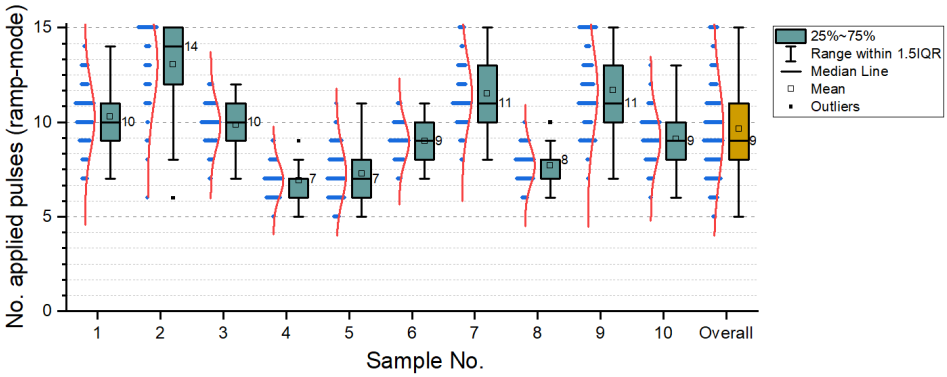

Fig. 4. Number of applied pulses in ramp-mode (max. 15 pulses) within the RFD probe regions until the automated treatment laser interruption based on detected fringe washouts in OCT M-scans by the dosimetry algorithm (blue dots: number of applied pulses; red distribution curve). Across all samples, the median number of ramp pulses applied was 9 out of 15.

Fig. 5 shows the resulting RPE lesion sizes in the RFD probe region after fully automated treatment laser interruption. Overall, a mean lesion size of 8074 µm^2 was found which corresponds well to the initial treatment laser spot size of 90×90 µm^2 (8100 µm^2).

As depicted in Fig. 6(a), for the single pulse probe regions (P1 and P2), the rmcorr coefficient (r_{rm}) indicates a strong relationship between the achieved lesion size on the RPE and the applied treatment pulse energy, ($r_{rm} = 0.92$, 95%-CI *[0.90, 0.94]*). For the RFD probe regions, the correlation coefficient for repeated measures reveals only a moderate relationship between the RPE lesion size and the applied ramp end energy, respectively the number of applied pulses

Biomedical Optics EXPRESS

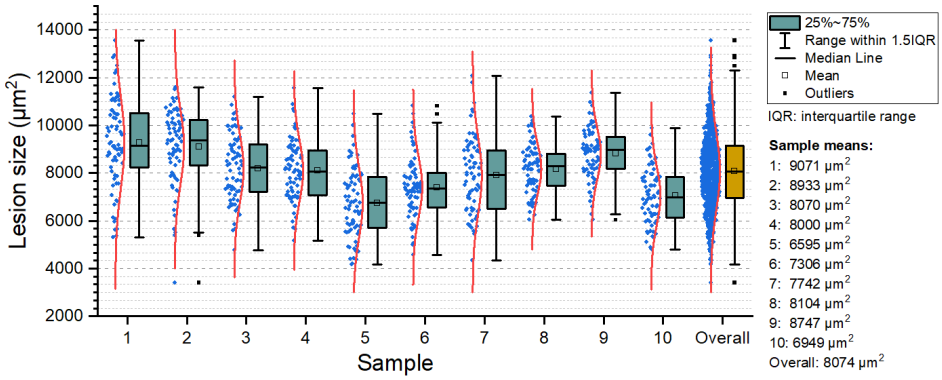

Fig. 5. Measured lesion sizes per sample for the RFD probe region based on the RPE cell viability assay (blue dots: lesion sizes; red distribution curve). Overall, a mean lesion size of 8074 µm^2 was found. IQR: interquartile range.

in ramp-mode, ($r_{rm} = 0.56$, 95%-CI *[0.51, 0.61]*). The moderate dependency is shown in the corresponding scatterplot (Fig. 6(b)).

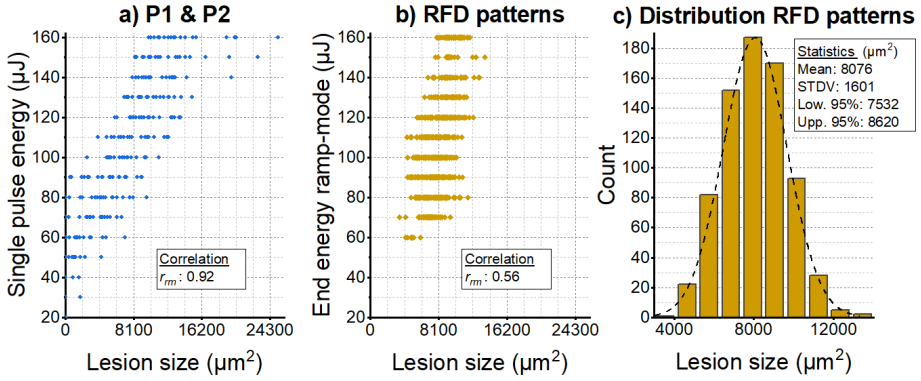

Fig. 6. Scatter diagrams showing the linear and monotonic relationship between the applied pulse energy and the resulting RPE lesion sizes for the single pulse probe regions P1 and P2 (a) and RFD patterns (b). (c) distribution of measured lesion sizes in the RFD patterns. STDV: standard deviation; Low. and Upp. 95%: lower and upper 95% confidence interval of mean.

A standard deviation of 1601 µm^2 was found for the distribution of the measured lesion RPE lesion sizes in the RFD probe regions (Fig. 6(c)). The 80% prediction interval, adjusted for the repeated measurements within a sample, is [6304, 9953]. That means that with 80% certainty a future lesion size would be between 6304 µm^2 and 9953 µm^2. The mean and the corresponding 95% confidence interval is 8076 µm^2 ([7532, 8620]). Therefore, with certainty 95%, the true mean laser lesion size is within this interval. The observed mean of 8076 µm^2 almost perfectly corresponds to the treatment laser spot size on the retina of the porcine eyes of 8100 µm^2.

Fig. 7 shows a detailed evaluation of a single sample (sample No. 5). The color-coded map in the RFD region (Fig. 7(g)) indicates that in the left region the treatment laser was deactivated at a lower end energy (around 70 µJ; 6/15 pulse) while in the right region a higher end energy (around 100 µJ; 9/15 pulse) was applied. However, as can be seen in Fig. 7(a), despite the different end energies, the generated RPE lesions were always of approximately the same lateral extent (Fig. 7(i)). Fig. 7(d) shows an exemplary evaluation for a lesion from the RFD pattern

Biomedical Optics EXPRESS

(No. 5). As shown in Fig. 7(e), a fringe washout was detected for this lesion in the OCT M-scan at pulse 7/15 (Fig. 7(f)). Thus, a final energy of 80 µJ (total energy applied to the tissue: 440 µJ) was applied. Within the ramp, this corresponds to a total of 33% of the maximum possible energy (1350 µJ). The RFD algorithm thus successfully created an RPE lesion, while avoiding 67% of the energy (910 µJ) to be applied, thus preventing suprathreshold treatment effects in the sense of SRT.

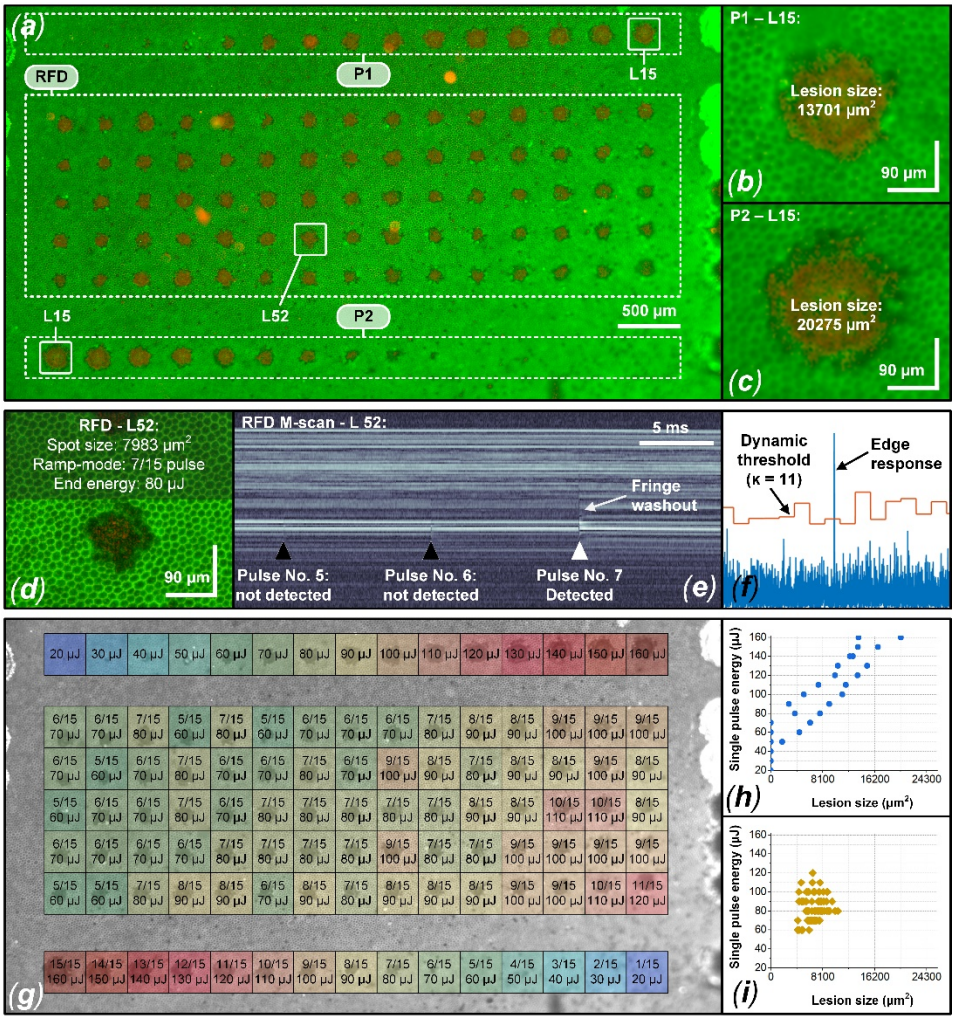

Fig. 7. (a) live/dead RPE cell viability assay and RFD evaluation of sample No. 5 (1-163) showing the two single pulse probe regions (P1 and P2) as well as the RFD probe region. (b, c) RPE lesions at maximum treatment energy with a damage area extending the treatment spot size (8100 µm^2) likely due to thermal diffusion. (d-f) exemplary OCT M-scan evaluation of lesion No. 52 from the RFD pattern. For this lesion, the RFD algorithm detected a fringe washout at pulse No. 7 / 15. (g) overview RFD region with color coding according to the applied ramp end energy and applied pulses, respectively. Correlation between RPE spot size and applied energy within the single pulse probe region (h) and RFD pattern (i)

As described previously, the dosimetry algorithm was only actively applied to the RFD probe region. However, post-treatment the theoretical algorithm performance was also determined for the single pulse probe regions P1 and P2. Therefore, the OCT M-scans recorded during the

Biomedical Optics EXPRESS

single pulse laser application were validated for the initial sensitivity setting of $\kappa = 11$ (RFD preset) as well as 18 other κ-value settings. Table 1 shows the results of this evaluation whereas for each sample the best result at the optimal κ-value setting for this sample is shown.

Table 1. Post-treatment algorithm fringe washout SD-OCT M-scan analysis of the single pulse probe region (P1 and P2)

Sample	κ-value	TP	TN	FP	FN	PPV	NPV	Sens.	Spec.	Acc.
1	9	14	14	0	2	1.00	0.88	0.88	1.00	0.93
2	9	14	13	0	3	1.00	0.81	0.82	1.00	0.90
3	11	17	12	0	1	1.00	0.92	0.94	1.00	0.97
4	9	19	7	2	2	0.90	0.78	0.90	0.78	0.87
5	10	18	12	0	0	1.00	1.00	1.00	1.00	1.00
6	10	18	10	0	2	1.00	0.83	0.90	1.00	0.93
7	10	13	15	0	2	1.00	0.88	0.87	1.00	0.93
8	10	18	10	0	2	1.00	0.82	0.90	1.00	0.93
9	10	7	17	0	6	1.00	0.74	0.54	1.00	0.80
10	9	15	13	0	2	1.00	0.87	0.88	1.00	0.93
RFD preset[a]	11	145	124	1	30	0.99	0.81	0.83	0.99	0.90
Overall[b]	10	150	123	2	25	0.99	0.83	0.86	0.98	0.91

TP: true positive; TN: true negative; FP: false positive; FN: false negative; PPV: positive predictive value; NPV: negative predictive value; Sens.: sensitivity; Spec.: specificity; Acc.: accuracy.
[a](RFD preset): overall evaluation based on the κ-value preset of 11 which was used for the RFD pattern.
[b](Overall): overall evaluation based on the median κ-value of 10 found over all samples.

The highest accuracy of 100% was achieved for sample No. 5 and $\kappa = 10$. In this case, only TP and TN events were identified by the OCT feedback algorithm, resulting in a sensitivity and specificity of 100%. The lowest accuracy of 80% was achieved for sample No. 9 and $\kappa = 10$. A total of 6 FN events lead to a relatively low sensitivity of 54%. The overall evaluation using the κ-value preset of 11 used for RFD (Table 1: RFD preset) resulted in an overall accuracy of 90% if applied to the single pulse probe regions P1 and P2. Across all samples, a median κ-value of 10 was found to be optimal. Using this κ-value, an accuracy of 91%, a sensitivity of 86%, and a specificity of 98% were achieved across all damage threshold patterns.

OCT C-scans across the patterns helped to assess possible retinal perturbation after laser application. An exemplary OCT B-scan post-treatment morphological tissue assessment based on sample No. 5 is shown in Fig. 8. Thereby, we focused on the ellipsoid zone (EZ), formerly known as the inner/outer segment of photoreceptors (IS/OS), and the area up to the outer plexiform layer (OPL) (Fig. 8(c); yellow delimitation). For the single pulse probe regions (P1 and P2), a slight hyperreflectivity was found in some cases for higher pulse energies. For the RFD probe region, no morphologic change (no layer upward protrusion or disturbed layer continuity) was observed in the choroid nor the entire retina, up to the internal limiting membrane (ILM). No thickening and hyperreflectivity was present in the EZ region and outer nuclear layer (ONL). The RPE / Bruch's membrane (BM) / choriocapillaris (CC) complex showed continuous reflectivity.

Biomedical Optics EXPRESS

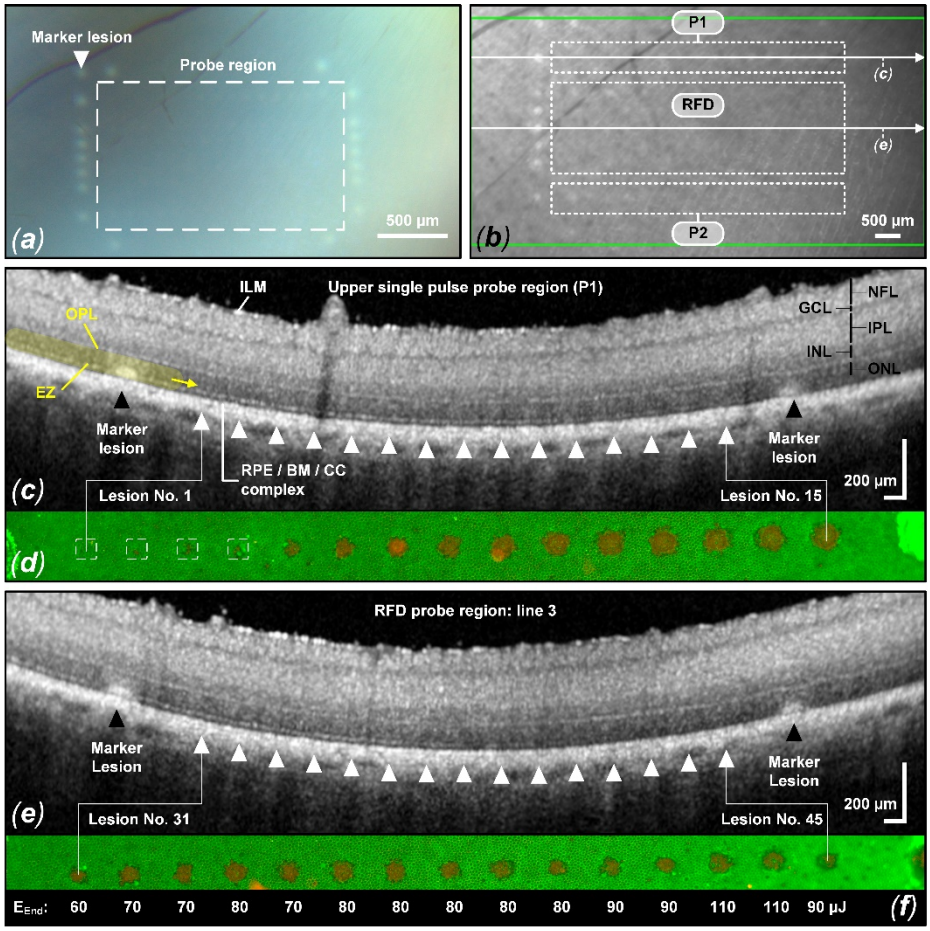

Fig. 8. Exemplary OCT B-scan post-treatment tissue assessment of sample No. 5 (1-163). (a) CFP image showing 19 marker lesions around the SRT probe region. (b) corresponding IR cSLO image (30°) of the pig fundus. The green rectangle marks the 30°× 15° OCT C-scan area which includes 145 B-scans with 30 µm horizontal spacing. For each B-scan, 34 scans were averaged for improved image quality. (c) OCT B-scan trough the upper single pulse probe region and corresponding live/dead RPE cell viability assay (d). (e) scan trough line three of the RFD probe region (lesion 31-45) and corresponding live/dead RPE cell viability assay with RFD end energies (f). Apart from the marker lesions, the retina shows no abnormalities in the area of the photoreceptors, except for partially subtle hyperreflectivity. Morphological porcine retina assessment according to Xie et al. [72]: retinal layers are marked by ILM: inner limiting membrane; NFL: nerve fiber layer; GCL: ganglion cell layer; IPL: inner plexiform layer; INL: inner nerve fiber layer; OPL: outer plexiform layer; ONL: outer nuclear layer; EZ: ellipsoid zone; RPE: retinal pigment epithelium; BM: Bruch's membrane; CC: choriocapillaris.

Biomedical Optics EXPRESS

4. Discussion

In this study, OCT-based RFD to selectively destroy RPE cells was investigated for the first time in a large pattern (15 × 5 lesions) implementing SRT. Therefore, laser pulses of 8 µs duration were applied in ramp-mode (15 pulses, 100 Hz repetition rate) with increasing radiant exposure to ex vivo porcine eyes. Furthermore, inter- and intraindividual RPE damage thresholds were investigated based on two locally separated single pulse probe regions.

As shown in Fig. 3, only in one of ten samples (sample No. 7) the same RPE damage threshold of 100 µJ (1235 mJ/cm^2) was observed across the two horizontally separated (≈2 mm) single pulse probe regions P1 and P2. All other samples revealed different RPE damage thresholds. The largest intraindividual variation of +/-20%, corresponding to a difference of 40 µJ (494 mJ/cm^2) was found for sample No. 1. Across all samples, the maximum required RPE damage threshold exceeded the minimum by a factor of 2. The absolute pulse energy difference was even as high as 60 µJ (741 mJ/cm^2). Considering the therapeutic window (TW; ratio between overtreatment (ophthalmoscopy) and undertreatment (angiography)) of factor 1.7 found by Framme et al. in the treatment of patients with macular disorders with laser pulses of 1.7 µs duration (wavelength: 527 nm) [73], the importance of RFD to adjust the laser pulse energy inter- and intra-individually to counteracting conditions such as different ocular transmission and RPE melanin concentration becomes evident. Especially if the even higher pigmentation variation of the human fundus by a up to a factor of 3.2 between the macula and far-periphery is considered [34]. Even in the currently investigated samples a wider test area than just ≈2 mm would unveil a much larger maximum difference than just 40 µJ for a given eye due to the stronger pigmentation variability, emphasizing the importance of RFD for SRT and basically any type of laser application to the retina.

For eyes in which a high RPE damage threshold was found (i.e. Sample No. 9: 100 µJ (P1); 120 µJ (P2)), lesions with high ramp end energy (median: 11/15 pulses, 120 µJ) tended to be applied in the RFD sample region. In contrast, eyes with a low RPE damage threshold (i.e. Sample No. 8: 60/70 µJ) tended to have lesions with low ramp end energy applied (median: 8/15 pulses, 90 µJ). Thus, the RFD apparently adapts to the conditions (transmission in the ocular medium, RPE absorption) and thus seems to reliably control SRT.

The results of the calcein-AM assay underline the necessity of RFD for SRT. In accordance with a similar experiment performed by Burri et al. [54] as well as Schuele et al. [74] on RPE-sclera-choroid explants, we observed a large difference between the ED_{16} and ED_{84} RPE damage threshold values (ED_{16} = 66 µJ, ED_{84} = 107 µJ, ΔQ = 41 µJ (506 mJ/cm^2). Regarding the evaluation of our porcine retinas, practically all samples showed local radiant exposure RPE damage threshold variability (Fig. 3). This variation may be related to local differences in the melanin distribution of the RPE as well as to differences in ocular transmission.

As expected, a significant strong correlation between the applied laser pulse energies and the resulting lesion size was found for the single pulse probe regions (P1 and P2). In the RFD probe region, however, there is only a moderate correlation between the lesion size and the applied pulse number respectively the applied end energy in ramp mode. Thus, using RFD, lesions are generated that were almost always the same size. In this respect, it is proven that our OCT-based RFD algorithm adapts to the local conditions and applies the appropriate laser pulse energy intraindividually.

In this experiment, the working range for the ramp-mode was chosen very large with a starting energy of 20 µJ (247 mJ/cm^2) and end energy of 160 µJ (1975 mJ/cm^2) in order to test RFD as broadly as possible. In a clinical setting, this range is usually narrowed down based on previously applied titration spots. In our ongoing patient study (CENTAURUS), for example, we set the end energy to 80% of the indications for suprathreshold effects (ophthalmoscopic visible) found by single pulse titration spots. Thereby, the starting energy is set as 20% of the end energy. Other groups limited the ramp's range even more by setting the start energy as 50% of the end energy,

Biomedical Optics EXPRESS

resulting in a much smaller working range [75]. We therefore expect an even better performance for our RFD if this methodology would also be applied. In this experiment, however, the goal was not to control the RPE threshold as precisely as possible, but to show how the SD-OCT-based RFD acts and adapts within the ramp.

As a preset for the RFD experiments, a κ-value setting of 11 was chosen for the OCT dosimetry algorithm. The selection of this value was based on previous experiments and experience. However, the results shown in Table 1 for the evaluation of the single pulse probe regions (P1 and P2) indicate that a median κ-value of 10 would have been better suitable across all 10 samples. Therefore, this algorithm setting might have led to even better results. However, Table 2 also shows that different κ-values would have proved optimal across all samples. The κ-values found ranged from 9 to 11. For clinical application, it could therefore be advantageous to adjust the algorithm settings individually for each eye or even each lesion. An individual dosimetry setting could for example be based on an OCT SNR measurement. However, for this kind of experiment, the settings of the algorithm were chosen almost perfectly in the sense that the mean lesion size of 8074 μm^2 found in the RFD probe region corresponds almost exactly to the measured laser spot size of 8100 μm^2.

Compared to other RFD methods evaluated for SRT (i.e. optoacoustics), we see a major advantage of OCT dosimetry in the contactless application and thus the massively improved patient comfort. The cumbersome application of an additional sensor to measure optoacoustic signals is unnecessary and would increase the risk of ocular irritation. Another aspect, namely sustainability in medicine aims to reduce disposables. Large amounts of waste are already being generated by sterilely packaged disposable products for many treatments. In this respect, we also see an advantage in OCT dosimetry, which does not require a contact glass and can be easily reused, thereby improving the economic and ecological profile of this minimally invasive procedure.

Besides the application to enable SRT, OCT is also evaluated as dosimetry tool (thermometry of ocular tissues) for photothermal laser therapies aiming to induce a specific temperature increase in the tissue (hyperthermia) as well as for controlling the degree of coagulation in classical laser photocoagulation (LPC). By using high speed (215 kHz A-scan rate) real-time OCT M-scans, Müller et al. [42] already tried to visualize retinal continuous-wave LPC (wavelength: 532 nm; radiant power: 3–130 mW; exposure: 50–400 ms) by monitoring thermal tissue expansion and scattering changes over longer time-scales. They found an increased hyperreflectivity (ΔS) in the photoreceptor layer by up to 8 dB following laser application. Furthermore, retinal surface displacements in the order of 60 µm could be detected. These effects in OCT M-scans increased more or less in parallel with increasing coagulation temperature, whereas they measured increased peak temperatures up to 50 K by optoacoustics. However, in the presented experiment and as depicted in Fig. 9, no tissue expansion during SRT and only a minimal change in scattering behavior in the photoreceptor region of 1 dB was found. At the temporal M-scan location where fringe washouts occur, signal losses were evident, although being rather weak washouts at the RPE damage threshold. These results suggest that, as intended for SRT, using pulse bursts and a relatively low repetition rate of 100 Hz at pulse durations shorter than the theory-derived thermal relaxation time for RPE cells (10 µs) [15], there are no cumulative thermal effects in the tissue whilst only high peak temperatures appear trigger MBF and RPE damage. This also corresponds to our latest ex vivo porcine eye experiment where cumulative RPE damage could be excluded for pulse durations of 8 and 12 µs applied in ramp-mode [76].

As a competitive approach, Lee et al., recently demonstrated swept-source OCT based SRT dosimetry on ex vivo bovine retinas [77]. They measured the speckle-variance (SV) within OCT M-scans that were recorded simultaneously to the treatment laser application. They previously evaluated this method for using SV-OCT to monitor thermally induced protein denaturation and coagulation processes on egg white proteins [78]. Typically, SV-OCT is one method to

Biomedical Optics EXPRESS

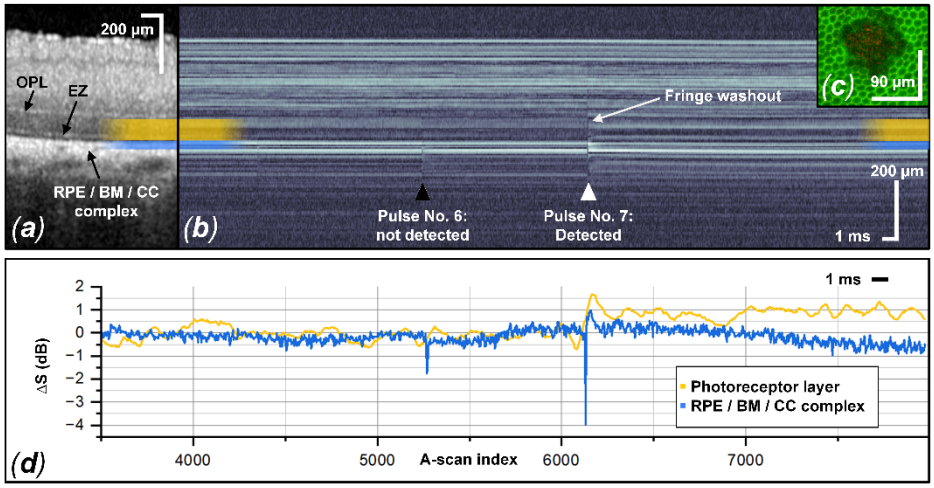

Fig. 9. Thermal tissue expansion and scattering change during SRT for lesion No. 52 from the RFD pattern of sample No. 5.: (a) post-treatment OCT B-scan at the laser treatment location of lesion No. 52. (b) corresponding OCT M-scan acquired during laser application. (c) complementary live/dead RPE cell viability assay of lesion No. 52. (d) change in hyperreflectivity (ΔS) within EZ and the area up to the OPL (yellow) as well as the RPE / Bruch's membrane (BM) / choriocapillaris (CC) complex for the in depicted M-scan.

visualize retinal micro vasculatures and capture functional images of blood flow, a technique known as OCT angiography (OCT-A) [79,80]. SV-OCT quantifies the variation of the coherence induced micropattern caused by changing interference of moving particles or deformations. By comparing an OCT image sequence of a microscopically static structure the interframe intensity variance is evaluated. Currently, imaging artifacts such as physiologic eye motion imitate OCT-A [81] and consequently SV-OCT based SRT dosimetry performance. Involuntary eye movements (e.g., micro saccades and drifts [82]) remain a major cause of artifacts even for ultrahigh-speed OCT systems [83,84]. While this approach is similar to the M-scan-method, the extension across one or even two spatial dimensions dramatically increases the requirements to acquisition speeds multiple orders higher than in the static, single depth scan position method. For OCT-A eye movements are much more likely to hinder clinical application. Furthermore, memory and processing bandwidth-hungry post-processing algorithms or precise and ultra-fast active eye tracking has to be used to superimpose images for evaluation. Implementation of SRT dosimetry requires real-time decisions and responses, which is probably much more difficult to implement in an image-based approach, rather than the one presented here.

The IR cSLO images, which were taken after laser application, showed a pronounced hyperreflectivity for marker lesions (Fig. 2(a, b)), depending on the angle of exposure. However, within the single pulse and RFD sample regions, we found no immediate change in reflectivity in this experiment. The same was already observed by us [48–50] as well as by Binter et al. in patients treated with SRT [85]. In their study, SRT lesions appeared after one week in IR images. This observation is related to local hyperreflectivity and thickening at the level of the RPE in OCT B-scan images, possibly indicating focal proliferation [85] of the RPE in the process of lesion closure after laser treatment (RPE rejuvenation). The changes in OCT morphology decreased and normalized within 6 months, and the neurosensory retinal layers, including the outer photoreceptor layers, appeared to be largely unaffected in all SRT lesions. In this respect, the immediate laser action on the porcine eye fundus in this ex vivo experiment shows parallels to patient studies.

Biomedical Optics EXPRESS

Recently, the Spectralis Centaurus device was used at a pulse duration of 8 µs in an in vivo rabbit model to remove the RPE over a large area, allowing for a simplified subretinal injection [86]. This procedure should one day benefit RPE cell therapies and remove the host RPE cells prior to the injection of new stem cell–derived RPE cells. In this experiment, we had set the target energy for large area RPE removal to a fixed value, based on titration lesions. Consequently, within the large treatment area of up to 13.6 mm^2, subthreshold as well as slightly suprathreshold effects occurred in part due to the local differences in absorption properties. Using the RFD approach shown here, large-area RPE removal would overcome these adverse side-effects, and thus make this elegant preparation step for RPE cell suspension even safer.

5. Limitations

The apparent adaptation of our RFD algorithm to the respective local conditions such as ocular transmission and RPE pigmentation cannot be demonstrated with this experiment. With respect to RPE pigmentation, a technology such as transscleral optical phase imaging (TOPI) would have to be used (i.e. Cellularis, EarlySight, CH). TOPI relies on high-angle oblique illumination (transscleral flood illumination) of the retina, combined with adaptive optics, to enhance cell contrast [87]. This cellular-resolution label-free high-contrast images would allow for fully automated RPE cell quantification by means of density, area, pigmentation, etc. [87–89]. Thereby, a weak RPE pigmentation should lead to a high end-energy and a strong pigmentation to a correspondingly low ramp end-energy determined by the SRT dosimetry algorithm. Unfortunately, this novel technology was not available for this experiment.

As already mentioned in our latest publication [76], a limitation of our ex vivo porcine eye experiments can of course be related to the ex vivo experimental setting. Although the eyes were treated as soon as possible after enucleation, the intraocular pressure was maintained and the cornea was moistened, the thermodynamic processes may have been different from an in vivo situation. The for the transport cooled and subsequently at room temperature (≈21°C) treated eyes had a different baseline temperature compared to the in vivo body temperature (≈37°C). Furthermore, there is no heating (cooling) by blood circulation an no metabolic heat generation. Thus, there is a different heat flow and possibly also a heat accumulation in the retina that would take place differently in vivo. However, we also already showed results from in vivo rabbit and pig experiments with successful RFD using OCT in smaller patterns as well as the possibility of RFD OCT in the CENTAURUS patient study (ClinicalTrials.gov Identifier: NCT04968756). Therefore, it can be assumed that the present results may also be representative of the in vivo situation.

Another limitation, which is also due to the ex vivo setting, was the OCT quality. In the OCT-B scans shown here, it is evident that despite the short time between enucleation and treatment, the retina had already begun to retain water (edema formation). As a result, the retinal structures were significantly worse to assess than one would expect from an in vivo situation. Therefore, morphologic changes were difficult to detect in OCT B-scans. Furthermore, this circumstance has a negative impact on the performance of the RFD algorithm, since a good SNR is important to reliably detect fringe washouts in OCT M-scans. In this respect, even better OCT dosimetry feedback can be expected in an in vivo setting.

6. Conclusion

Our results demonstrate that selective RPE photodisruption can be reliably controlled using OCT-based dosimetry. Statistical analysis reveals a moderate correlation between RPE lesion size and applied treatment energy, suggesting intraindividual adaptation to RPE pigmentation and ocular transmission by RFD. RPE lesion sizes are well controlled and homogeneous over large patterns. In addition, no signs of suprathreshold treatment effects were found by means of OCT and CFP in the SRT sample region controlled with RFD after laser exposure. The method

Biomedical Optics EXPRESS

is directly translatable to in vivo applications, where we expect to achieve similar precision. It should guarantee the reproducibility of SRT treatment spots and ensures the safety of retinal laser treatments by fully automated patient and lesion-specific end energy adjustment. Future research still must verify whether real-time OCT dosimetry in patients undergoing SRT is capable of automatically controlling the level of treatment to induce RPE regeneration without any adverse effects on neighboring tissue.

Acknowledgments. We gratefully want to acknowledge the valuable support and the inspiring discussions with our colleagues from Heidelberg Engineering and Meridian Medical.

Disclosures. C.B. Meridian Medical (F,E,R), Heidelberg Engineering (F,R); The remaining authors declare no potential conflicts of interest.

Data availability. Data underlying the results presented in this paper are not publicly available at this time but may be obtained from the authors upon reasonable request - excluding the SD-OCT dosimetry algorithm.

References

1. E. Szalai, J. M. Nickerson, and H. E. Grossniklaus, "RPE histopathology and morphometry," in *Retinal Pigment Epithelium in Health and Disease*, A. K. Klettner and S. Dithmar, eds. (Springer Cham, 2020).
2. R. J. Sparrow, D. Hicks, and P. C. Hamel, "The retinal pigment epithelium in health and disease," Curr. Mol. Med. **10**(9), 802–823 (2010).
3. J. B. Hurley, "Retina metabolism and metabolism in the pigmented epithelium: a busy intersection," Annu. Rev. Vis. Sci. **7**, 665–692 (2021).
4. P. Röhlich, "The interphotoreceptor matrix: Electron microscopic and histochemical observations on the vertebrate retina," Exp. Eye Res. **10**(1), 80–86 (1970).
5. L. J. Rizzolo, "RPE polarity and barrier function," in *Retinal Pigment Epithelium in Health and Disease*, A. K. Klettner and S. Dithmar, eds. (Springer Cham, 2020).
6. O. Strauss, "The retinal pigment epithelium in visual function," Physiological Reviews **85**(3), 845–881 (2005).
7. R. W. Young, "Visual cells, daily rhythms, and vision research," Vision Res. **18**(5), 573–578 (1978).
8. S. Grisanti, "Das Immunprivileg des Auges," Ophthalmologe **95**(2), 124–135 (1998).
9. M. Chen and H. Xu, "Parainflammation, chronic inflammation, and age-related macular degeneration," Journal of Leukocyte Biology **98**(5), 713–725 (2015).
10. A. K. Klettner, "Physiological functions of VEGF in the retina and its possible implications prolonged anti-VEGF therapy," in *Vascular Endothelial Growth Factor (VEGF): Biology, Regulation and Clinical Significance*, M. L. Parker, ed. (Nova Publishing, 2013).
11. M. Boulton and P. Dayhaw-Barker, "The role of the retinal pigment epithelium: Topographical variation and ageing changes," Eye **15**(3), 384–389 (2001).
12. C. Framme, A. Walter, L. Berger, P. Prahs, C. Alt, D. Theisen-Kunde, J. Kowal, and R. Brinkmann, "Selective retina therapy in acute and chronic-recurrent central serous chorioretinopathy," Ophthalmologica **234**(4), 177–188 (2015).
13. H.-Z. Xu, Z. Song, S. Fu, M. Zhu, and Y.-Z. Le, "RPE barrier breakdown in diabetic retinopathy: seeing is believing," Journal of Ocular Biology, Diseases, and Informatics **4**(1-2), 83–92 (2011).
14. J. Tode, Y. Miura, R. Brinkmann, and C. Von der Burchard, "Retina regenerative laser and light therapies (RELITE): - a new nomenclature and trial reporting standard proposal," Investigative Ophthalmology and Visual Science **64**, (2023).
15. R. Brinkmann, J. Roider, and R. Birngruber, "Selective retina therapy (SRT): a review on methods, techniques, preclinical and first clinical results," Bulletin de la Société belge d'ophtalmologie **302**, 51–69 (2006).
16. J. Roider, F. Hillenkamp, T. Flotte, and R. Birngruber, "Microphotocoagulation: selective effects of repetitive short laser pulses," Proc. Natl. Acad. Sci. U.S.A. **90**(18), 8643–8647 (1993).
17. V. P. Gabel, R. Birngruber, and F. Hillenkamp, "Visible and near infrared light absorption in pigment epithelium and choroid," XXIII Concilium Ophthalmology Kyoto (1978).
18. J. Neumann and R. Brinkmann, "Boiling nucleation on melanosomes and microbeads transiently heated by nanosecond and microsecond laser pulses," J. Biomed. Opt. **10**(2), 024001 (2005).
19. J. Neumann and R. Brinkmann, "Cell disintegration by laser-induced transient microbubbles and its simultaneous monitoring by interferometry," J. Biomed. Opt. **11**(4), 041112 (2006).
20. A. Fritz, L. Ptaszynski, H. Stoehr, and R. Brinkmann, "Dynamics of laser induced transient micro bubble clusters," in *Therapeutic Laser Applications and Laser-Tissue Interactions IV*, R. Sroka and L. Lilge, eds. (Optica Publishing Group, Munich, 2009).
21. Y. G. Park, J. R. Kim, S. Kang, E. Seifert, D. Theisen-Kunde, R. Brinkmann, and Y.-J. Roh, "Safety and efficacy of selective retina therapy (SRT) for the treatment of diabetic macular edema in Korean patients," Graefe's Arch. Clin. Exp. Ophthalmol. **254**(9), 1703–1713 (2016).
22. M. Kim, Y. G. Park, S. H. Jeon, S. Y. Choi, and Y.-J. Roh, "The efficacy of selective retina therapy for diabetic macular edema based on pretreatment central foveal thickness," Lasers Med Sci **35**(8), 1781–1790 (2020).

Biomedical Optics EXPRESS

23. J. Roider, S. H. M. Liew, C. Klatt, H. Elsner, E. Poerksen, J. Hillenkamp, R. Brinkmann, and R. Birngruber, "Selective retina therapy (SRT) for clinically significant diabetic macular edema," Graefe's Arch. Clin. Exp. Ophthalmol. **248**(9), 1263–1272 (2010).
24. M. Yamamoto, Y. Miura, K. Hirayama, T. Kohno, D. Kabata, D. Theisen-Kunde, R. Brinkmann, and S. Honda, "Predictive factors of outcome of selective retina therapy for diabetic macular edema," Int. Ophthalmol. **40**(5), 1221–1232 (2020).
25. M. Yamamoto, Y. Miura, K. Hirayama, A. Kyo, T. Kohno, D. Theisen-Kunde, R. Brinkmann, and S. Honda, "Comparative treatment study on macular edema secondary to branch retinal vein occlusion by intravitreal ranibizumab with and without selective retina therapy," Life **13**, 769 (2023).
26. M. Buettner, B. Luger, W. Abou Moulig, B. Junker, C. Framme, C. Jacobsen, K. Knoll, and A. Pielen, "Selective retina therapy (SRT) in patients with therapy refractory persistent acute central serous chorioretinopathy (CSC): 3 months functional and morphological results," Graefe's Arch. Clin. Exp. Ophthalmol. **259**(1), 1–10 (2021).
27. H. Elsner, E. Porksen, C. Klatt, A. Bunse, D. Theisen-Kunde, R. Brinkmann, R. Birngruber, H. Laqua, and J. Roider, "Selective retina therapy in patients with central serous chorioretinopathy," Graefe's Arch. Clin. Exp. Ophthalmol. **244**(12), 1638–1645 (2006).
28. A. Yasui, M. Yamamoto, K. Hirayama, K. Shiraki, D. Theisen-Kunde, R. Brinkmann, Y. Miura, and T. Kohno, "Retinal sensitivity after selective retina therapy (SRT) on patients with central serous chorioretinopathy," Graefe's Arch. Clin. Exp. Ophthalmol. **255**(2), 243–254 (2017).
29. A. Kyo, M. Yamamoto, K. Hirayama, T. Kohno, D. Theisen-Kunde, R. Brinkmann, Y. Miura, and S. Honda, "Factors affecting resolution of subretinal fluid after selective retina therapy for central serous chorioretinopathy," Sci Rep **11**(1), 8973 (2021).
30. S. Kang, Y. G. Park, J. R. Kim, E. Seifert, D. Theisen-Kunde, R. Brinkmann, and Y. J. Roh, "Selective retina therapy in patients with chronic central se-rous chorioretinopathy: a pilot study," Medicine **95**(3), e2524 (2016).
31. C. Klatt, M. Saeger, T. Oppermann, E. Pörksen, F. Treumer, J. Hillenkamp, E. Fritzer, R. Brinkmann, R. Birngruber, and J. Roider, "Selective retina therapy for acute central serous chorioretinopathy," Br. J. Ophthalmol. **95**(1), 83–88 (2011).
32. M. Kim, Y. G. Park, and Y.-J. Roh, "One-Year Functional and Anatomical Outcomes After Selective Retina Therapy With Real-Time Feedback-Controlled Dosimetry in Patients With Intermediate Age-Related Macular Degeneration: A Pilot Study," Lasers Surg. Med. **53**, 499–513 (2021).
33. S. K. Bhatia, A. Rashid, M. A. Chrenek, Q. Zhang, B. B. Bruce, M. Klein, J. H. Boatright, Y. Jiang, H. E. Grossniklaus, and J. M. Nickerson, "Analysis of RPE morphometry in human eyes," Mol. Vis. **22**, 898–916 (2016).
34. S. Y. Schmidt and R. D. Peisch, "Melanin concentration in normal human retinal pigment epithelium. Regional variation and age-related reduction," Investigative Ophthalmology and Visual Science **27**, 1063 (1986).
35. J. J. Weiter, F. C. Delori, G. L. Wing, and K. A. Fitch, "Retinal pigment epithelial lipofuscin and melanin and choroidal melanin in human eyes," Inv. Ophthal. Vis. Sci. **27**, 145–152 (1986).
36. J. Dillon, L. Zheng, J. C. Merriam, and E. R. Gaillard, "Transmission of light to the aging human retina: possible implications for age related macular degeneration," Exp. Eye Res. **79**(6), 753–759 (2004).
37. L. Kessel, J. H. Lundeman, K. Herbst, T. V. Andersen, and M. Larsen, "Age-related changes in the transmission properties of the human lens and their relevance to circadian entrainment," Journal of Cataract and Refractive Surgery **36**(2), 308–312 (2010).
38. G. Schuele, H. Elsner, C. Framme, J. Roider, R. Birngruber, and R. Brinkmann, "Optoacoustic real-time dosimetry for selective retina treatment," J. Biomed. Opt. **10**(6), 064022 (2005).
39. E. Seifert, Y.-J. Roh, A. Fritz, Y. G. Park, S. Kang, D. Theisen-Kunde, and R. Brinkmann, "Automatic irradiation control by an optical feedback technique for selective retina treatment (SRT) in a rabbit model," in *Medical Laser Applications and Laser-Tissue Interactions VI*, L. Lilge and R. Sroka, eds. (Optica Publishing Group, Munich, 2013).
40. D. Huang, E. A. Swanson, C. P. Lin, J. S. Schuman, W. G. Stinson, W. Chang, M. R. Hee, T. Flotte, K. Gregory, C. A. Puliafito, and J. G. Fujimoto, "Optical Coherence Tomography," Science **254**(5035), 1178–1181 (1991).
41. L. M. Sakata, J. DeLeon-Ortega, V. Sakata, and C. A. Girkin, "Optical coherence tomography of the retina and optic nerve – a review," Clinical and Experimental Ophthalmology **37**, 90–99 (2009).
42. H. H. Müller, L. Ptaszynski, K. Schlott, C. Debbeler, M. Bever, S. Koinzer, R. Birngruber, R. Brinkmann, and G. Hüttmann, "Imaging thermal expansion and retinal tissue changes during photocoagulation by high speed OCT," Biomed. Opt. Express **3**(5), 1025 (2012).
43. P. Steiner, V. Enzmann, C. Meier, B. Považay, and J. Kowal, "Retinal Laser Lesion Visibility in Simultaneous Ultra-High Axial Resolution Optical Coherence Tomography," IEEE Photonics J. **6**(6), 1–11 (2014).
44. P. Steiner, A. Ebneter, L. E. Berger, M. Zinkernagel, B. Považay, C. Meier, J. Kowal, C. Framme, R. Brinkmann, S. Wolf, and R. Sznitman, "Time-Resolved Ultra–High Resolution Optical Coherence Tomography for Real-Time Monitoring of Selective Retina Therapy," Investigative Ophthalmology and Visual Science **56**(1), 1–9 (2015).
45. P. Steiner, B. Považay, M. Stoller, P. Morgenthaler, D. Inniger, P. Arnold, R. Sznitman, and C. Meier, "Real-time optical coherence tomography observation of retinal tissue damage during laser photocoagulation therapy on ex-vivo porcine samples," in *Optical Coherence Imaging Techniques and Imaging in Scattering Media*(Optica Publishing Group, Munich, 2015).

Biomedical Optics EXPRESS

46. C. Burri, A. Hutfilz, L. Grimm, S. Salzmann, P. Arnold, B. Považay, C. Meier, A. Ebneter, D. Theisen-Kunde, and R. Brinkmann, "Dynamic OCT Signal Loss for Determining RPE Radiant Exposure Damage Thresholds in Microsecond Laser Microsurgery," Appl. Sci. **11**(12), 5535 (2021).
47. C. Burri, B. Stanzel, A. Schweri-Olac, S. Al-Nawaiseh, P. Wakili, G. Farese, S. Salzmann, B. Považay, C. Meier, M. Frenz, A. Schulz, and V. Enzmann, "Histologic findings following retinal pigment epithelium removal using 8 microsecond laser pulses," in Proc. SPIE (2023).
48. C. Burri, C. Dysli, S. Salzmann, B. Povazay, C. Meier, M. Frenz, S. Zinkernagel, and S. Wolf, "Dosimetry of selective retina therapy using optical coherence tomography: first results from the CENTAURUS study," Inv. Ophthal. Vis. Sci. **64**, 1800 (2023).
49. C. Dysli, C. Burri, S. Salzmann, B. Povazay, C. Meier, M. Frenz, M. S. Zinkernagel, and S. Wolf, "Optical Coherence Tomography Guided Selective Retina Therapy: First results from the CENTAURUS study," Inv. Ophthal. Vis. Sci. **64**, 1804 (2023).
50. C. Dysli, C. Burri, S. Salzmann, B. Povazay, M. Christoph, F. Martin, M. S. Zinkernagel, and S. Wolf, "High resolution optical coherence tomography reveals details of regeneration after selective retina therapy," Inv. Ophthal. Vis. Sci. **64**, PB0052 (2023).
51. C. Burri, S. Al-Nawaiseh, A. Schulz, P. Wakili, G. Farese, P. Szurman, S. Salzmann, R. Brinkmann, B. Povazay, C. Meier, M. Frenz, and B. V. Stanzel, "Real-Time Optical Coherence Tomography Controlled Microsecond Laser Retinal Microsurgery: First In-vivo Results," Inv. Ophthal. Vis. Sci. **63**, 3796 (2022).
52. M. Evers Olufsen, C. Burri, S. Salzmann, B. Povazay, C. Meier, M. Frenz, and J. F. Kiilgaard, "In-vivo Real-Time Feedback-Controlled Dosimetry of Microsecond Laser Retinal Microsurgery using Optical Coherence Tomography," Inv. Ophthal. Vis. Sci. **64**, 1801 (2023).
53. J. F. Bille, *High Resolution Imaging in Microscopy and Ophthalmology* (Springer International Publishing, 2019).
54. C. Burri, A. Hutfilz, L. Grimm, P. Arnold, R. Brinkmann, D. Theisen-Kunde, A. Ebneter, B. Považay, and C. Meier, "Optical coherence tomography controlled selective retina therapy with a novel microsecond laser," in *Clinical and Preclinical Optical Diagnostics II*(Optica Publishing Group, Munich, 2019).
55. A. Hutfilz, C. Burri, D. Theisen-Kunde, C. Meier, and R. Brinkmann, "Ex-vivo investigation of different µs laser pulse durations for selective retina therapy," in *Clinical and Preclinical Optical Diagnostics II*(Optica Publishing Group, Munich, 2019).
56. C. Framme, G. Schuele, J. Roider, D. Kracht, R. Birngruber, and R. Brinkmann, "Threshold Determinations for Selective Retinal Pigment Epithelium Damage With Repetitive Pulsed Microsecond Laser Systems in Rabbits," Ophthalmic Surgery, Lasers and Imaging Retina **33**(5), 400–409 (2002).
57. Z. Y. Li, F. Wong, J. H. Chang, D. E. Possin, Y. Hao, R. M. Petters, and A. H. Milam, "Rhodopsin transgenic pigs as a model for human retinitis pigmentosa," Inv. Ophthal. Vis. Sci. **39**, 808 (1998).
58. D. R. Bertschinger, E. Beknazar, M. Simonutti, A. B. Safran, J. A. Sahel, S. G. Rosolen, S. Picaud, and J. Salzmann, "A review of in vivo animal studies in retinal prosthesis research," Graefes Arch. Clin. Exp. Ophthalmol. **246**(11), 1505–1517 (2008).
59. Y. Miura, "Retinal pigment epithelium–choroid organ culture," Expert Rev. Ophthalmol. **6**(6), 669–680 (2011).
60. M. J. Chandler, P. J. Smith, D. A. Samuelson, and E. O. MacKay, "Photoreceptor density of the domestic pig retina," Vet. Ophthalmol. **2**(3), 179–184 (1999).
61. C. Kostic and Y. Arsenijevic, "Animal modelling for inherited central vision loss," J. Pathol. **238**, 300–310 (2016).
62. J. Ruiz-Ederra, M. Garcia, M. Hernandez, H. Urcola, E. Hernandez-Barbachano, J. Araiz, and E. Vecino, "The pig eye as a novel model of glaucoma," Experimental Eye Research **81**(5), 561–569 (2005).
63. Y. X. Wang, L. Xu, W. B. Wei, and J. B. Jonas, "Intraocular pressure and its normal range adjusted for ocular and systemic parameters. The Beijing Eye Study 2011," PLoS One **13**(5), e0196926 (2018).
64. S. D'Souza, S. Annavajjhala, P. Thakur, R. Mullick, S. J. Tejal, and N. Shetty, "Study of tear film optics and its impact on quality of vision," Indian J. Ophthalmol. **68**(12), 2899–2902 (2020).
65. P. E. King-Smith, B. A. Fink, N. Fogt, K. K. Nichols, R. M. Hill, and G. S. Wilson, "The Thickness of the Human Precorneal Tear Film: Evidence from Reflection Spectra," Inv. Ophthal. Vis. Sci. **41**, 3348–3359 (2000).
66. P. E. King-Smith, S. H. Kimball, and J. J. Nichols, "Tear Film Interferometry and Corneal Surface Roughness," Invest. Ophthalmol. Vis. Sci. **55**(1), 1 (2014).
67. M. Garca, J. Ruiz-Ederra, H. Hernandez-Barbachano, and E. Vecino, "Topography of pig retinal ganglion cells," J. Comp. Neurol. **486**, 361–372 (2005).
68. I. Sanchez, R. Martin, F. Ussa, and I. Fernandez-Bueno, "The parameters of the porcine eyeball," Graefe's Archive for Ophthalmology **249**(1), 1–2 (2011).
69. J. Schindelin, I. Arganda-Carreras, E. Frise, V. Kaynig, M. Longair, T. Pietzsch, S. Preibisch, C. Rueden, S. Saalfeld, B. Schmid, J. Tinevez, D. White, V. Hartenstein, K. Eliceiri, P. Tomancak, and A. Cardona, "Fiji: an open-source platform for biological-image analysis," Nat. Methods **9**(7), 676–682 (2012).
70. D. H. Sliney, J. Mellerio, V. P. Gabel, and K. Schulmeister, "What is the meaning of threshold in laser injury experiments? Implications for human exposure limits," Health Phys. **82**(3), 335–347 (2002).
71. J. Z. Bakdash and L. R. Marusich, "Repeated Measures Correlation," Front. Psychol. **8**, 456 (2017).
72. W. Xie, M. Zhao, S.-H. Tsai, W. L. Burkes, L. B. Potts, W. Xu, H. R. Payne, T. W. Hein, L. Kuo, and R. H. Rosa, "Correlation of spectral domain optical coherence tomography with histology and electron microscopy in the porcine retina," Exp. Eye Res. **177**, 181–190 (2018).

Biomedical Optics EXPRESS

73. C. Framme, A. Walter, P. Prahs, D. Theisen-Kunde, and R. Brinkmann, "Comparison of threshold irradiances and online dosimetry for selective retina treatment (SRT) in patients treated with 200 nanoseconds and 1.7 microseconds laser pulses," Lasers Surg. Med. **40**, 616–624 (2008).
74. G. Schuele, M. Rumohr, G. Huettmann, and R. Brinkmann, "RPE damage thresholds and mechanisms for laser exposure in the microsecond-to-millisecond time regimen," Invest. Ophthalmol. Vis. Sci. **46**(2), 714–719 (2005).
75. E. Seifert, J. Tode, A. Pielen, D. Theisen-Kunde, C. Framme, J. Roider, Y. Miura, R. Birngruber, and R. Brinkmann, "Selective retina therapy: toward an optically controlled automatic dosing," Journal of Biomedical Optics **23**(11), 1 (2018).
76. C. Burri, S. Salzmann, M. Amstutz, L. Hoffmann, B. Považay, C. Meier, and M. Frenz, "Investigation of the Influence of Pulse Duration and Application Mode on Microsecond Laser Microsurgery of the Retinal Pigment Epithelium," Life **13**(6), 1314 (2023).
77. S. Lee, S. Wei, S. Guo, J. Kim, B. Kim, G. Kim, and J. Kang, "Selective retina therapy monitoring by speckle variance optical coherence tomography for dosimetry control," J. Biomed. Opt. **25**(02), 1–9 (2020).
78. C. Lee, G. Cheon, D.-H. Kim, and J. U. Kang, "Feasibility study: protein denaturation and coagulation monitoring with speckle variance optical coherence tomography," J. Biomed. Opt. **21**(12), 125004 (2016).
79. M. S. Mahmud, D. W. Cadotte, B. Vuong, C. Sun, T. W. H. Luk, A. Mariampillai, and V. X. D. Yang, "Review of speckle and phase variance optical coherence tomography to visualize microvascular networks," J. Biomed. Opt. **18**(5), 050901 (2013).
80. I. Gorczynska, J. V. Migacz, R. J. Zawadzki, A. G. Capps, and J. S. Werner, "Comparison of amplitude-decorrelation, speckle-variance and phase-variance OCT angiography methods for imaging the human retina and choroid," Biomed. Opt. Express **7**, 1 (2016).
81. J. L. Lauermann, M. Treder, P. Heiduschka, C. R. Clemens, N. Eter, and F. Alten, "Impact of eye-tracking technology on OCT-angiography imaging quality in age-related macular degeneration," Graefe's Arch. Clin. Exp. Ophthalmol. **255**(8), 1535–1542 (2017).
82. S. Martinez-Conde, S. L. Macknik, and D. H. Hubel, "The role of fixational eye movements in visual perception," Nature Reviews Neuroscience **5**(3), 229–240 (2004).
83. T. Klein, W. Wieser, C. M. Eigenwillig, B. R. Biedermann, and R. Huber, "Megahertz OCT for ultrawide-field retinal imaging with a 1050 nm Fourier domain mode-locked laser," Opt. Express **19**(4), 3044 (2011).
84. B. Potsaid, I. Gorczynska, V. J. Srinivasan, Y. Chen, J. Jiang, A. Cable, and J. G. Fujimoto, "Ultrahigh speed Spectral / Fourier domain OCT ophthalmic imaging at 70,000 to 312,500 axial scans per second," Opt. Express **16**(19), 15149 (2008).
85. M. Binter, M. Lindziute, C. Rosenstein, C. Framme, and J. Tode, "Long-Term Multimodal Imaging Analysis of Selective Retina Therapy Laser Lesions," Life **13**(4), 886 (2023).
86. C. Burri, S. Al-Nawaiseh, P. Wakili, S. Salzmann, C. Krotz, B. Povazay, C. Meier, M. Frenz, P. Szurman, A. Schulz, and B. Stanzel, "Selective Large-Area Retinal Pigment Epithelial Removal by Microsecond Laser in Preparation for Cell Therapy," Trans. Vis. Sci. Tech. **10**(10), 17 (2021).
87. T. Laforest, M. Kunzi, L. Kowalczuk, D. Carpentras, F. Behar-Cohen, and C. Moser, "Transscleral Optical Phase Imaging of the Human Retina," Nat. Photonics **14**(7), 439–445 (2020).
88. F. L. Caetano Dos Santos, T. Laforest, M. Künzi, L. Kowalczuk, F. Behar-Cohen, and C. Moser, "Fully automated detection, segmentation, and analysis of in vivo RPE single cells," Eye **35**(1), 1–3 (2021).
89. L. Kowalczuk, R. Dornier, M. Kunzi, A. Iskandar, Z. Misutkova, A. Gryczka, A. Navarro, F. Jeunet, I. Mantel, F. Behar-Cohen, T. Laforest, and C. Moser, "In Vivo Retinal Pigment Epithelium Imaging using Transscleral Optical Imaging in Healthy Eyes," Ophthalmology Science **3**(1), 100234 (2023).